Evolution dynamics of discrete-continuous light bullets

Falk Eilenberger,[1] Stefano Minardi,[1] Alexander Szameit,[1,2] Ulrich Röpke,[3] Jens Kobelke,[3] Kay Schuster,[3] Hartmut Bartelt,[3]
Stefan Nolte,[1] Lluis Torner,[4] Falk Lederer,[5] Andreas Tünnermann,[1] and Thomas Pertsch[1]

[1]*Institute of Applied Physics, Friedrich-Schiller-Universität Jena, Max-Wien-Platz 1, D-07743 Jena, Germany*

[2]*Department of Physics, Solid State Institute, Technion-Israel Institute of Technology, 32000 Haifa, Israel*

[3]*Institute of Photonic Technology, Albert-Einstein-Strasse 9, D-07745 Jena, Germany*

[4]*ICFO-Institut de Ciences Fotoniques, and Universitat Politecnica de Catalunya, Mediterrean Technology Park,*
E-08860 Castelldefels (Barcelona), Spain

[5]*Institute of Condensed Matter Theory and Solid State Optics, Friedrich-Schiller-Universität Jena, Max-Wien-Platz 1,*
D-07743 Jena, Germany

We experimentally and numerically investigate the propagation of light bullets (LBs) excited in two-dimensional fiber arrays. The combination of nonlinear self-frequency shift, wavelength dependence of the dispersion, and the interwaveguide coupling strength induce an adiabatic variation of the parameters of the LBs along their propagation paths, until they reach the limits of the regime of existence and decay. The relative strength of the various perturbative effects can partially be controlled by the array's geometry. The characterization of the LB dynamics is carried out by implementing a spatiotemporal, cross-correlating, and spectrally resolved imaging system with femtosecond resolution. The experimental results are in good agreement with the numerical data if higher-order nonlinear effects and the wavelength dependence of the dispersion and coupling are included. The observed wave packets are linked to the stationary solutions of the simplified nonlinear Schrödinger equation. Furthermore, the maximum possible range of existence of LBs in arrays of waveguides is discussed.

I. INTRODUCTION

In the past three decades, considerable effort has been devoted to the investigation of optical solitary waves [1,2] due to their fundamental impact on nonlinear wave propagation, spawning exciting applications on the way, such as supercontinuum light sources [3], soliton lasers [4], and an improved understanding of the development and control of rogue waves [5]. Solitary waves are wave packets that balance linear dispersive and/or diffractive broadening with the nonlinear response of the optical medium. Their particlelike behavior makes them a formidable subject for the study of wave propagation in nonlinear media and suitable elements to deliver and process quantized packets of energy.

Starting with the investigation of solitons in optical fibers [1,6,7], research has diversified [2] also addressing optical solitary waves in higher-dimensional media, which display a more complex phenomenology due to the increased degrees of freedom [8].

In this context, the generation, the observation, and the control of wave packets that are simultaneously nondispersive and nondiffractive in bulk optical media (the so-called light bullets (LBs) [9]) have been long-lasting challenges in nonlinear optics. In fact, LBs in pure Kerr media are unstable, i.e., small perturbations lead either to spreading or to catastrophic collapse of the wave packet. However, theoretical research has pointed out that stable LBs may be observed in media featuring different types of nonlinearity [10–14] and/or in microstructured media [15–19].

Despite considerable theoretical work, experimental research lagged behind, mainly due to the fact that detrimental higher-order nonlinear effects are not negligible because existing materials are only weakly dispersive and cause LBs to be extremely short.

Considerable advances toward the generation of LBs have been achieved in $\chi^{(2)}$ media, where two-color spatiotemporal solitons [20,21] have been observed with a tilted pulse [22,23]. In these experiments, pulse tilting was required to achieve group-velocity matching between nonlinearly coupled harmonics and to induce an unusually high level of effective anomalous dispersion. However, this technique is limited to a single effective transverse dimension. The generalization of the technique for two transverse dimensions leads to the generation of so-called X-waves, i.e., wave packets featuring an angularly dispersed spatiotemporal spectrum with axial symmetry. X-waves can be generated spontaneously in $\chi^{(2)}$ [24,25] or $\chi^{(3)}$ media [26,27] but feature a weak spatiotemporal localization of light and a theoretically infinite energy content due to the slowly decaying wings of the wave packet. Also of infinite energy content are linear LBs, which are a spatiotemporal superposition of nondiffracting and nondispersing Airy and/or Bessel beams [28,29].

Another approach, which has been investigated experimentally, is the nonlinear propagation of ultrashort pulses in transversally structured optical lattices. These media support not only nonlinear lattice X-waves [30,31], but also stable lattice solitons in one or two spatial dimensions [32–36] featuring improved stability properties over their homogeneous counterparts, including LBs [9,16–18,37,38]. Until recently, the experimental characterization of nonlinear spatiotemporal pulse evolution in structured $\chi^{(3)}$ media did not produce a clear identification of LBs [39–41] due to limitations of the diagnostic tools used for spatiotemporal characterization. Improved characterization techniques based on the spatially resolved cross-correlation method [24,25, 42–44] allowed us recently to identify LBs [45] excited in highly regular two-dimensional arrays of coupled waveguides [46,47].

In Ref. [45], we reported that the excited wave packets propagate as LBs for many dispersion lengths while experiencing self-frequency shift and adiabatic adaptation to changing dispersion conditions. This evolution process lasts until the energy budget of the LBs is no longer sufficient to support nonlinear confinement against the growing dispersion and diffraction strength.

In this paper, we address, in more detail, the propagation of LBs by providing additional experimental data, and we provide an analysis of the parameters controlling the existence range of the LBs.

The paper is set up as follows. In Sec. II, we give an overview of the properties of the waveguide array and idealized discrete-continuous bullet solutions of the nonlinear Schrödinger equation (NLSE). In Sec. III, we summarize the experimental results of the paper, reporting the observation of LBs, and we describe the linear dispersive properties of the waveguide arrays. We present experimental data for waveguide arrays featuring reduced coupling strength as compared to previous experiments. In the following Sec. IV, we explain the observed phenomena with the help of numerical simulations based on the unidirectional Maxwell equations and discuss the wave-packet evolution dynamics by relating them to adiabatically evolving LB solutions of the NLSE. The consequences of our findings on the extension of the stability and the existence range of the LB are then presented in the concluding Sec. V. A summary of the experimental as well as the numerical methods are included in the Appendices.

II. OVERVIEW OF THE PHYSICAL SYSTEM

Nonlinear light propagation in arrays of coupled waveguides entails a complex dynamics, which can be understood by means of the concept of discrete-continuous LB and the knowledge of higher-order linear and nonlinear properties of the array. In this section, we summarize the properties of the array and ideal discrete-continuous LB solutions, presenting the definition of quantities that are relevant for the interpretation of the experiments.

A. Properties of the array of waveguides

We investigate light propagation in arrays of evanescently coupled single-mode fiber cores, a sample of which is depicted in Fig. 1(a). They have been fabricated by a rod-in-tube process [46,47] of fluorine-doped tubes placed around pure silica cores with special boundary rods to ensure a high quality of the array all the way to the edges. Their high degree of regularity is reflected by the high symmetry of the linear discrete diffraction pattern, depicted in Fig. 1(b). This allows for neglecting effects, which stem from stochastic variations of the interwaveguide coupling across the array [36,48,49].

Linear properties of the infinite array are determined by numerical simulation of the band structure of a homogenous circular rod with a refractive index $n(\omega)$ embedded in the center of a hexagonal unit cell. The background refractive index is lowered to $n(\omega) - \Delta n$ where ω is the angular carrier frequency related to the wavelength by $\omega = 2\pi V/\lambda$ with the speed of light V. The index difference between the core and the background is nondispersive at $\Delta n = 1.1 \times 10^{-3}$ whereas,
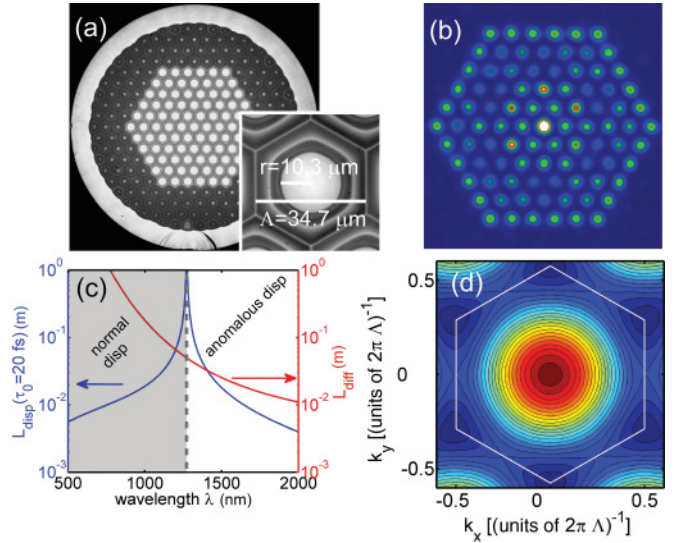

FIG. 1. (Color online) Linear properties of a typical fiber array. (a) Image of the front facet of a fiber array with a unit cell pitch of $\Lambda = 34.7$ μm and a core radius of $r = 10.3$ μm. (b) Linear diffraction pattern of the array depicted in (a). (c) Linear length scales of the array depicted in (a) as a function of the wavelength. (Blue) The dispersion length for a pulse with $\tau_0 = 20$ fs. The gray section on the left marks the normal dispersion range, whereas, the white section to the right marks the anomalous dispersion regime, which supports bright LB solutions for $n_2 > 0$. (Red) The discrete diffraction length for the array depicted in (a) as a function of the wavelength. (d) Band structure of the Bloch modes of an infinitely extended array. The first Brillouin zone is marked with the white line.

the base refractive index is modeled with chromatic dispersion using the Sellmeier equation and tabulated data for fused silica [1].

A typical isofrequency curve (band structure of the first Brillouin zone at a fixed frequency) is shown in Fig. 1(d). The band structure can be fitted to an analytic expression [50], yielding the propagation constant of the fundamental guided mode of an individual waveguide $\beta_0(\omega)$ and the interwaveguide coupling strength $c(\omega)$ which describes the discrete diffraction. These two quantities determine the linear spatial and temporal evolution lengths L_{Diff} and L_{Disp}, respectively. They are defined as

$$L_{\text{Diff}}(\omega) = \frac{\pi}{2\sqrt{6}c(\omega)},$$
$$L_{\text{Disp}}(\omega) = \frac{\tau_0^2}{|\beta_2(\omega)|},$$

where τ_0 is the $1/e$ width of a pulse, with the carrier frequency ω and $\beta_2(\omega) = d^2\beta/d\omega^2$ is the group-velocity dispersion (second derivative of the propagation constant with respect to the angular frequency). If it is positive, one speaks of normal dispersion and of anomalous dispersion otherwise. A typical wavelength dependence of these parameters is plotted in Fig. 1(c). Note that, in the anomalous dispersion regime, both characteristic length scales decrease almost exponentially upon the increase in the wavelength, which is due to the increased material dispersion induced by the far-infrared

resonance of the host material and the exponential increase in the overlap of neighboring modes.

As discussed later in our paper, we have observed a significant spectral and temporal reshaping of the light pulses propagating in the array. Thus, for a given pulse, both L_{Diff} and L_{Disp} are not constant along the propagation coordinate. Thus, we define pulse-trajectory-averaged quantities to analyze the robustness of the solitonic propagation,

$$
\begin{aligned}
\langle L_{\text{Diff}} \rangle &= (z_2 - z_1)^{-1} \int_{z_1}^{z_2} \frac{\pi}{2\sqrt{6}c[\omega_c(\tilde{z})]} d\tilde{z}, \\
\langle L_{\text{Disp}} \rangle &= (z_2 - z_1)^{-1} \int_{z_1}^{z_2} \frac{\tau_0(\tilde{z})^2}{|\beta_2[\omega_c(\tilde{z})]|} d\tilde{z},
\end{aligned}
\tag{2}
$$

where $\omega_c(z)$ is the pulse's spectral center of gravity.

B. Properties of LBs

In a first approximation, light propagating in arrays of waveguides is described by the discrete-continuous NLSE [16]. See Appendix B and Fig. 2 for the equation and the relation of the normalized quantities to their physical counterparts used below.

This equation is known to support bright solitary solutions as discussed in Refs. [16,17,19] and as discussed in more detail in Appendix B. One finds a family of LBs by solving Eq. (B1) for stationary solutions with the ansatz $A_{nm}(Z) = A_{nm}^{(\text{stat})} \exp(ibZ)$ characterized by the nonlinear shift b of the propagation constant. Properties of this family are displayed in Fig. 2. Note that the family consists of two distinct sections— whereas, LBs with $b < 8.2$ are unstable as predicted by the Vakhitov-Kolokolov theorem [51] and are confirmed by linear stability analysis shown in Fig. 2(c); there is a regime of stable LB solutions for $b > 8.2$. This feature is a direct consequence of the periodicity of the array and extends over a finite range

of nonlinear parameters to a value b_{crit}, linked to a peak power P_{crit}, which depends on the modulation depth of the refractive index and is discussed below in Appendix B.

Similarly, there is a lower limit for the peak power of stable LBs,

$$
P_{\text{min}} \approx 14.5,
\tag{3}
$$

which is the peak power of the LB at the transition point between stable and unstable LBs at $b = 8.2$.

One interesting consequence of this behavior is that pulse widths of all stable LBs of this equation belong to a finite range and cannot be chosen arbitrarily. This behavior is in sharp contrast to solitons of the one-dimensional (1D) NLSE. The upper bound, which has already been found for 1D waveguide arrays [37], is the temporal width of the solutions at the point $b = 8.2$, where the solution originally stabilizes,

$$
T_{\text{FWHM}} \leqslant 0.46.
\tag{4}
$$

If transferred back into real-world quantities, one acquires a value of $T_{\text{FWHM}} < 22$ fs for a wavelength of $\lambda = 1550$ nm and the geometry depicted in Fig. 1 with $L_{\text{Diff}} = 22$ mm.

Consequentially, there is a lower threshold energy for the LB,

$$
E > E_{\text{min}} = 9.05,
\tag{5}
$$

below which no LB solutions exist. This is caused by the dimensionality of the system and cannot be observed in a 1D system.

Another feature is that all LB solutions have a characteristic and nearly constant ratio of dispersion to diffraction lengths. The diffraction length is given by Eq. (1) as $L_{\text{Diff}}^{(\text{LB})} = 0.64 \, c^{-1}$, whereas, an upper limit for the dispersion length is determined
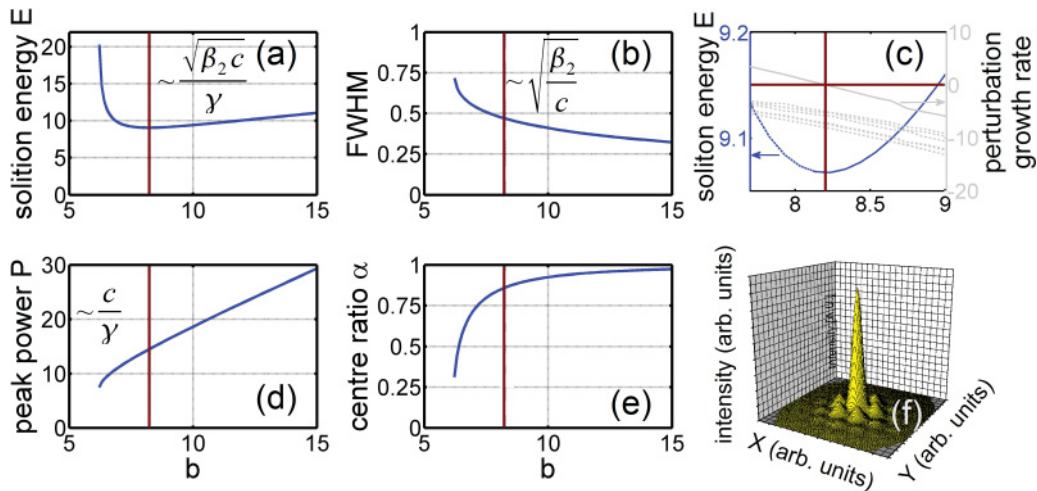

FIG. 2. (Color online) Family properties of LB solutions of Eq. (B1). (a) LB energy as a function of the nonlinear parameter b. (b) Temporal full width at half maximum (FWHM) of the pulse in the central waveguide. (c) Inset of (a) in the region close to the point of minimal energy. Shown are (blue, left axis) the energy of the LB and the largest real parts of the eigenvalues of the linear stability analysis (gray, right axis), whose sign determines the stability of the solution. (d) Peak power as a function of the nonlinear parameter. (e) The portion of the LB's energy that is guided in the central waveguide as a measure of spatial confinement. (f) The spatial energy distribution of the LB at the point with the lowest energy. The (vertical) red lines in (a)–(e) denote the border between stable and unstable LB solutions. The inset formulas relate the depicted normalized quantities to their physical counterparts.
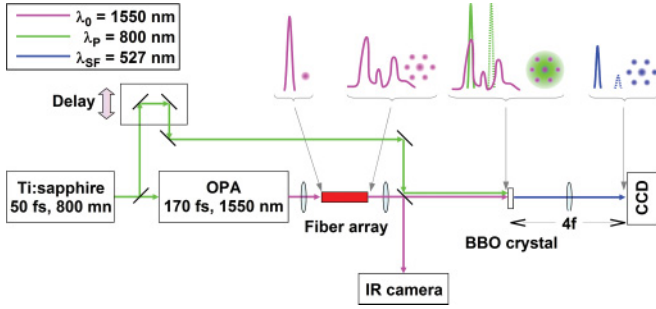
FIG. 3. (Color online) Pulses with a wavelength of 1550 nm from an optical parametrical amplifier (OPA), pumped by an 800 nm source (purple/gray) are launched into the central core of a fiber array. The resulting spatiotemporal light distribution is imaged onto a 10-μm-thin β-barium-borate (BBO) crystal where it is overlapped with a synchronized short and wide 800-nm pump pulse (green/light gray), with adjustable delay. A sum-frequency field (blue/dark gray) is generated at the overlap of the signal and pump pulse, which is proportional to the signal pulse at the time given by the delay. It is imaged onto a charge-coupled-device (CCD) camera, which records an image for each setting of the delay, thus, sampling the spatiotemporal intensity map of the signal with a temporal resolution on the order of the pump pulse width (60 fs). The pictures on top of the arrows are artist's impressions of the temporal and spatial light distributions at the points denoted thereby for different settings of the delay stage.

by the upper limit of the LB width in Eq. (4) as $L_{\mathrm{Disp}}^{(\mathrm{LB})} \leqslant 0.083\, c^{-1}$ Thus, one finds, for stable LB solutions,

$$L_{\mathrm{Diff}}^{(\mathrm{LB})} / L_{\mathrm{Disp}}^{(\mathrm{LB})} \approx 7.5, \tag{6}$$

which can be used to gauge whether wave packets are of solitary nature. Correspondingly, one can use Eq. (3) to find a maximum value for the nonlinear length,

$$L_{\mathrm{NL}}^{(\mathrm{LB})} = (cP)^{-1} \leqslant 0.07\, c^{-1}, \tag{7}$$

which is consistent with the assumption that, for solitary waves, the nonlinearity has to balance both the diffraction and the dispersion simultaneously, so L_{NL} has to be smaller than both L_{Diff} and L_{Disp} but not much smaller.

III. PHENOMENOLOGY OF LBS IN WAVEGUIDE ARRAYS

In recent experiments [45], we generated optical LBs by launching 170-fs pulses at $\lambda_0 = 1550$ nm into the central waveguide of a 91-element hexagonal array of coupled waveguides. The output pulse was characterized by means of an imaging cross-correlation technique [43,44] featuring 60-fs resolution. Figure 3 displays the experimental setup, which is explained in more detail in Appendix C, while Fig. 4 summarizes the observed phenomenology. At an input pulse energy of $E = 36$ nJ, spatiotemporal broadening is observed as expected for linear propagation. If the input power is increased to $E = 90$ nJ, an abrupt change takes place. A resolution-limited short pulse carrying much of the wave packet's energy is observed in the central waveguide of the array. In the spatiotemporal trace, one can clearly observe that the nonlinearly confined wave packet is spatiotemporally separated from weaker residual radiation, which diffracts. The wave packet arrives at a later time, suggesting that it is considerably redshifted, which is typical for solitary waves propagating under the influence of the Raman effect. At even higher input powers of $E = 180$ nJ, the spatial picture is mostly unchanged, but two temporally separated peaks are now observed in time, reminiscent of soliton splitting in ordinary optical fibers.

More information on the nature of the nonlinearly confined wave packets is given by the experimental cross-correlation-based frequency-resolved optical gating (XFROG) traces of the wave packets in the central waveguide. Figure 5 depicts measured and simulated traces at an input peak power of
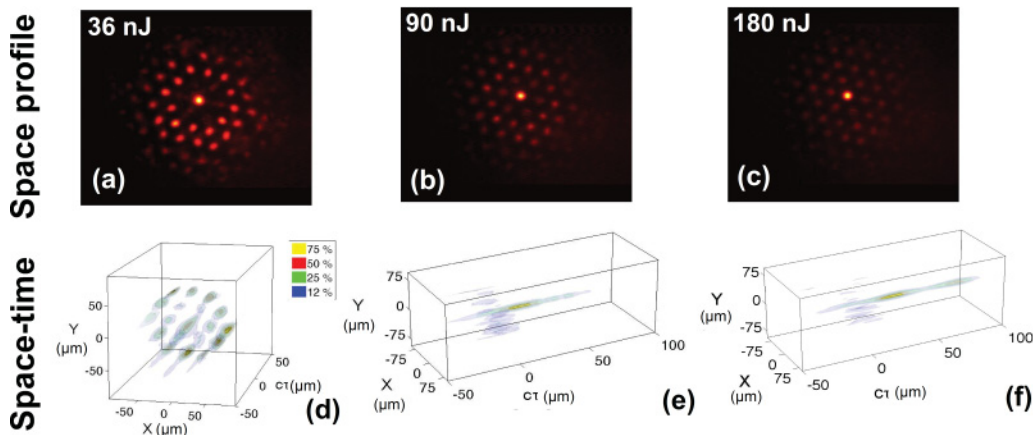

FIG. 4. (Color online) Results of light propagation through a fiber array with $L_{\mathrm{Diff}} = 22$ and $L = 40$ mm. (First row) Spatial distribution of power in the array. (Second row) Isointensity trace of the field at the end of the waveguide array, obtained from the cross-correlation setup. The isosurfaces correspond to the levels denoted in the legend of (d). (First column) Propagation at low power, exhibiting spatial and temporal broadenings. (Second column) Propagation at intermediate peak power. Most light is confined in the central waveguide, and considerable temporal contraction to the minimum temporal resolution of 60 fs is observed. A clear spatiotemporal separation of the nonlinearly confined wave packet and residual radiation is observed in the cross-correlation traces. (Third column) Propagation at higher powers. Similar to the intermediate case but two nonlinearly confined wave packets are observed. (Adapted from Ref. [45].)
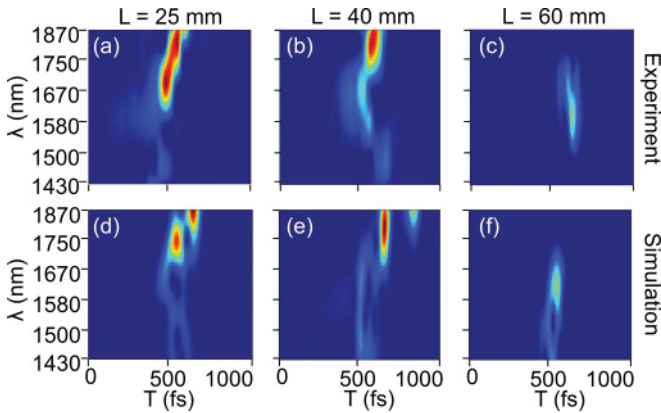
FIG. 5. (Color online) (Upper) Experimental and (lower) simulated XFROG traces of the field in the central waveguide. The initial peak power was $P_0 = 0.9$ MW, and $L_{Diff} = 22$ mm. Shown are sample lengths of (left) 25 mm, (middle) 40 mm, and (right) 60 mm. Note that there is no common color scale. The figures show the excitation of two heavily redshifted and delayed pulses at 25 mm. At 40 mm, the more heavily redshifted one has left the wavelength window, only the small part is still visible in the simulated data. Residual radiation with a shorter wavelength precedes the nonlinearly confined wave packets, which is the only detectable radiation left at 60 mm. (Adapted from Ref. [45].)

$P_0 = 0.9$ MW. At $z = 20$ mm, it shows the development and evolution of two distinct wave packets with a spectral FWHM of $\delta\lambda > 100$ nm, corresponding to a temporal FWHM of $\delta T < 20$ fs, indeed, much shorter than the resolution-limited information from the cross-correlation intensity plots and within the range of pulse widths expected for LBs given by

Eq. (4). The results are in excellent agreement with the synthetic XFROG traces calculated from numerical simulations based on the unidirectional Maxwell equations [52,53]. Both wave packets are continuously redshifted and consecutively slow down. At $z = 40$ mm, the stronger more redshifted wave packet has already left the experimental wavelength limit and is barely discernable at the border of the simulated one. Both pulses have disappeared at $z = 60$ mm, leaving only residual radiation in the central waveguide. Propagation lengths in between those depicted in Fig. 5 are shown in the corresponding movie, which displays the evolution of the XFROG trace for $z \leqslant 50$ mm. Note the striking agreement of measured and simulated data in both Figs. 4 and 5.

The complete evolution of the pulse in the central waveguide is depicted in Fig. 6(a). After the pulse initially contracts in time, it decays into multiple fragments, the first of which is clearly visible from $z = 15$ mm. It can be traced for a length of $L_{LB} = 25$ mm to $z = 40$ mm, where it decays rapidly. A second fragment, which develops at $z = 25$ mm, undergoes a similar evolution pattern. Figures 6(b) and 6(c) display the properties of the most redshifted pulse fragment. After strong temporal contraction, the pulse width settles at approximately 25 fs at $z = 15$ mm and starts to grow slowly from there. This slow broadening is not due to dispersion as displayed by the dotted line in Fig. 6(b), which represents dispersive broadening of a hypothetical pulse of the same width. The evolution is accompanied by a decelerating redshift, starting at $\lambda = 1600$ nm and ending at $\lambda = 1950$ nm, which is typical for the influence of self-induced Raman scattering. Note that, under the influence of linear discrete diffraction, blueshifting would be observed because the spectral components with longer wavelengths diffract faster (see Fig. 1).
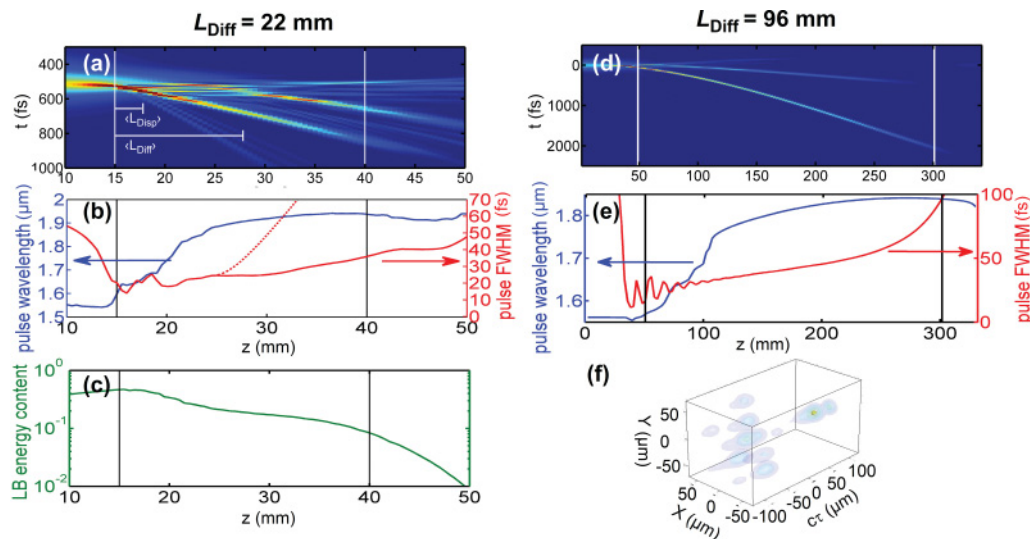

FIG. 6. (Color online) Pulse evolution in the central waveguide of a fiber array with (a)–(c) $L_{Diff} = 22$ mm with an input power of $P_0 = 0.9$ MW and (d)–(e) $L_{Diff} = 96$ mm with an input power of $P_0 = 50$ kW. (a) and (d) Power as a function of time and propagation length. (b) and (e) Pulse width (red/right axis) and pulse wavelength (blue/left axis) of the slowest most redshifted pulse fragment. (Red, dotted) Evolution of a hypothetical pulse of the same length as the observed wave packet, assuming purely linear dispersion. (c) The fraction of the total energy, which is confined in the central waveguide part of the slowest most redshifted pulse. The vertical lines in (a)–(c) denote the region of nonlinearly confined adiabatically redshifting pulse evolution. The pulse-averaged diffraction and dispersion lengths for this range are displayed in (a) and (d). (f) Experimental cross-correlation trace.
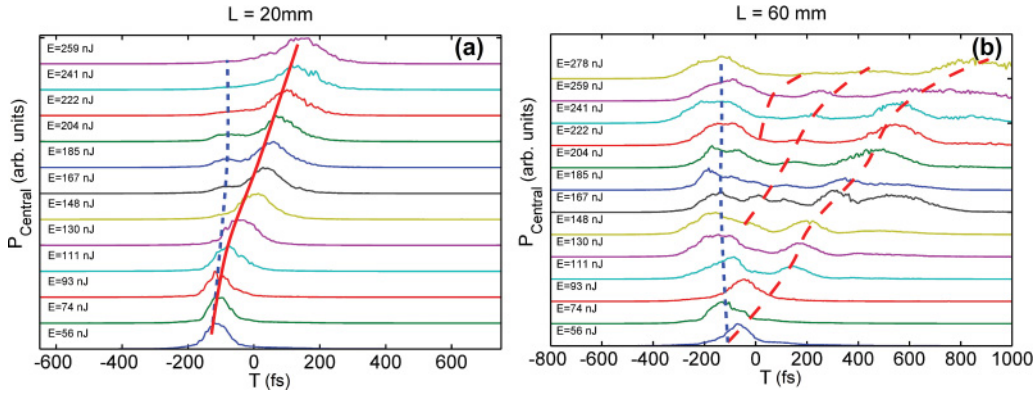
FIG. 7. (Color online) Cross-correlation measurements of the central waveguide of an array with $L_{\text{Diff}} = 22$ mm (a) after the point of creation of the first LB at $L = 20$ mm and (b) after the point of LB decay at $L = 60$ mm for various input intensities. Marked are (blue, small dashes) the dispersive wave peak, (red, solid) the LBs, and (red, large dashes) the residual leftovers of decayed LBs. (Media 1) [59] Movie of isointensity plots for the data depicted in (a). (Media 2) [59] Movie of isointensity plots for the data depicted in (b).

The energy content of the central waveguide component of the pulse is depicted in Fig. 6(c). After an initial content of roughly 40% at $z = 15$ mm, it slowly drops to about 15% at $z = 40$ mm. Note that this is not the total energy content of the nonlinearly confined pulse because the pulse also has a spatial structure and increasing energy content in the other waveguides.

Experimental support for these findings is given by data plotted in Fig. 7. It shows the power in the central waveguide as a function of the input energy for a sample length of $L = 20$ and $L = 60$ mm, respectively. It was obtained from the full cross-correlation data, which are displayed in (Media 1 and 2) [59]. A length of $L = 20$ mm was chosen to observe the state of the wave packet after the point of creation of the first LB. At this point, a single LB, which is redshifted if a higher input energy is applied, and a blueshifted broadened dispersive wave can be distinguished. The length of $L = 60$ mm lies beyond the point of LB decay. Nevertheless, some light of the former LBs has not yet tunneled out of the central waveguide and can clearly be observed as delayed pulses trailing the dispersive

waves. The number of delayed pulses grows if the input energy is increased.

IV. ADIABATIC LB EVOLUTION MECHANISM

The simulations reported in Fig. 6 prove the subdiffractive subdispersive properties of the observed localized wave packets but offer only an indirect link to the concept of LBs. The verification that adiabatically evolving LBs were indeed excited is given by Figs. 8(a) and 8(b). They show the pulse evolution of the strongest, most redshifted wave packets of the simulations depicted in Fig. 6 in the pulse's parameter space. This space is spanned by the pulse's central wavelength, its central waveguide energy content, and its FWHM pulse width during propagation. Depicted as well is the central waveguide energy of a LB solution of Eq. (B1) with the given FWHM and wavelength by the blue-red surface. This surface has been obtained by rescaling the results displayed in Fig. 2 to physical quantities, using the wavelength-dependent linear properties of the respective waveguide arrays as shown in Fig. 1.
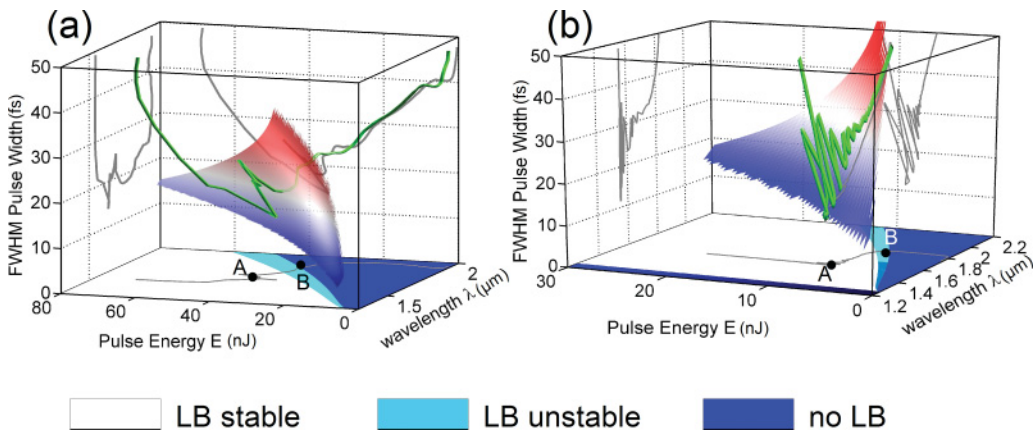

FIG. 8. (Color online) Adiabatic LB evolution in phase space for two different fiber geometries with (a) L_{Diff} (1550 nm) = 22 mm and (b) L_{Diff} (1550 nm) = 96 mm. The blue-red surface denotes the width of the LB solution of Eq. (B1), with the given pulse energy E and wavelength λ, transformed into real quantities, according to the fiber-array parameters. The green line is the evolution of the most redshifted pulse in parameter space. The gray lines are the green line's projection onto the coordinate surfaces. Points A and B mark the beginning and the end of the adiabatic evolution regime of the LB. (Media 3 and 4) [59] Animation of the pulse evolution for both array geometries.

The limits of nonlinearly confined behavior are marked with points A and B in the projection of the parameter curve onto the wavelength-energy plane. These points split the evolution into three distinct regimes. In the first regime, the pulse undergoes rapid nonlinear contraction and subsequent pulse splitting until one or more fragments of the pulse acquire a shape that is very close to the one defined by the surface. In the second regime, which has a length of $L_{LB} \approx 1.9\langle L_{Diff}\rangle = 9.0\langle L_{Disp}\rangle$, the wave packet propagates as such a LB, while the higher-order nonlinear terms lead to a slow redshift. The wave packets evolve adiabatically because the redshift imposes stronger coupling and dispersion. Although the LB's energy content is (almost) constant in physical units, it drops in normalized units. Eventually, it does not have enough normalized energy anymore to fulfill the existence criterion defined in Eq. (5) and, thus, decays. In Fig. 8, this point is marked by the motion of the parameter curve beyond the blue-red plane and by the crossing of the projected parameter curve into the blue region without LB solutions. Thus, the LB decay is not mediated by losses but by a slow evolution toward a state where the limited energy budget can no longer support solitary propagation.

A striking observation is the fact that the LB solutions of the simplified NLSE model are a useful tool at all for the description of the complex evolution mechanisms of ultrashort pulses in a heavily dispersive medium under the influence of higher-order linear and nonlinear terms, described by the much more complicated Eq. (C1). This underlines the potency of adiabatically evolving solitary solutions as a conceptual tool to describe and to understand nonlinear wave propagation phenomena in systems with a broad range of perturbations.

The question that naturally arises is whether the decay process of LBs could be slowed down by tuning the diffraction length. As outlined in Sec. IIB, a longer diffraction length implies a longer dispersion length, thus, LB solutions of longer pulse widths can be excited. As a consequence, higher-order effects are expected to be less relevant and possibly extending the life span of the bullet.

To verify this scenario, we investigate the formation and evolution of LBs in an array with a much larger diffraction length of $L_{Diff}(1550\ \mathrm{nm}) = 96$ mm. Results are depicted in Figs. 6(d)–6(f). After an initial phase of strong pulse contraction, multiple solitary wave packets are excited, which propagate, while slowly changing, until they decay. The slow evolution is related to a continuous redshift and subdispersive pulse broadening. The fragment is characterized by a pulse-averaged diffraction length $\langle L_{Diff}\rangle = 68.9$ mm and a dispersion length $\langle L_{Disp}\rangle = 10.3$ mm. Note that the ratio of both lengths is consistent with Eq. (6). Both are much shorter than the range of nonlinearly confined propagation. Figure 6(d) depicts the experimental cross correlation trace at $z = 160$ mm, which shows the nonlinearly confined wave packet trailing a well-separated linearly diffracting underground. The additional movie shows the evolution of the XFROG trace in the simulation. One interesting point, which can be observed in the movie, is that the most redshifted wave packet is unchirped, as expected for a LB. When, however, it starts to decay at $z = 300$ mm, an onset of linear-chirped broadening is clearly visible by the clockwise tilt of the pulse in the XFROG trace, consistent with the anomalous dispersion at this wavelength.

The length of confined propagation L_{LB} is approximately $L_{LB} \approx 3.5\langle L_{Diff}\rangle$ and $L_{LB} \approx 25\langle L_{Disp}\rangle$, roughly two to three times longer than that for the previously investigated $L_{Diff}(1550\ \mathrm{nm}) = 22$ mm-sample, suggesting a scaling of approximately $L_{LB}/\langle L_{Disp}\rangle \sim c^{-1/2}$. This behavior is consistent with the range of possible exponents derived from simple scaling laws, as predicted in Appendix D, Eq. (D4).

Although this is proof that a reduction in the coupling strength leads to an extension of the LB life span, this also shows that the influence is weak, scaling much slower than c^{-1} (see Appendix D). The ultimate limit to this scaling behavior is the length scale L_{Rand} at which variations in the waveguides lead to dephasing, and the linear propagation starts to be dominated by Anderson localization [36,48,49,54]. We estimate this length to be on the order of not much more than $L_{Rand} = 1$ m for our highly regular samples, limiting the nonlinear propagation to roughly $10\langle L_{Diff}\rangle$ or $100\langle L_{Disp}\rangle$.

Because any experimental system with nonlinear wave propagation will inevitably experience a certain level of redshift due to the noninstantaneous nonlinear response of the medium and some linear and/or nonlinear losses, we believe that the decay mechanism, which we have discussed, is of very generic nature for nonlinear self-confined wave-propagation phenomena. Thus, any LB in a real system will have a finite lifetime, after which it will inevitably decay. This mechanism can only be observed in high-dimensional systems, being in sharp contrast to the situation in integrable low-dimensional systems where infinite soliton propagation is, in principle, possible. Nevertheless, the understanding of the decay mechanism will greatly ease the development of systems with longer lived LBs, which would either have to experience less redshift or need to be designed to exhibit less wavelength dependence of the dispersive properties to withstand considerable redshift.

V. CONCLUSIONS

We have investigated nonlinear light propagation in arrays of evanescently coupled fiber arrays. The linear properties of the array have been carefully modeled to understand the dispersive and diffractive characteristics. A family of stationary solutions, termed LBs, has been investigated numerically. Important properties of this family have been thoroughly discussed, among which are ranges of stable solutions, energy and power thresholds, and a narrow window of possible pulse widths, which lies in the range of a few optical cycles for the properties of our experimental system. Keeping this finding in mind, we have expanded our model to numerically describe the propagation of such ultrashort excitations under the influence of the wavelength dependence of the dispersion, the interwaveguide coupling, and the noninstantaneous nonlinear response of the medium.

The results of the numerical simulation are in excellent agreement with various experiments in which we have used a cross-correlation technique to sample the spatiotemporal structure of the light field leaving the sample with a spatial resolution in the range of micrometers and a temporal resolution in the range of 60 fs, limited only by the pulse duration of the pump laser. A further modification of the

technique allows us to record spatiotemporal XFROG traces, giving insight into the wavelength structure of our pulse.

We find that the propagation can be split into three distinct regimes. In the first regime, the pulse undergoes strong nonlinear contraction and eventually splits into fragments. In the second regime, some of the fragments propagate nearly unchanged for many dispersion lengths. Their shape corresponds to the LB solutions of the simplified NLSE equation, although the system is heavily perturbed by nonlinear and linear effects of higher order. During this propagation, the wave packets undergo continuous redshift under the influence of the Raman effects, which forces the LBs to adapt to the changing dispersive properties of the medium. Eventually, the energy budget of the wave packet is insufficient to counteract the increasing dispersion and diffraction strength at longer wavelengths, and it decays quickly. We further argue that this decay mechanism is of generic nature for the propagation of solitary waves in higher-dimensional media, being only weakly dependent on the strength of the discrete diffraction.

APPENDIX A: EXPERIMENTAL SETUP AND IMAGING CROSS-CORRELATION SCHEME

The experimental setup is depicted in Fig. 3. The beam of a Ti:sapphire amplifier emitting 60-fs pulses at $\lambda_P = 800$ nm with a pulse energy of 0.6 mJ is split. Ninety percent is used to pump an OPA, which, in turn, is emitting 170-fs pulses at $\lambda_0 = 1550$ nm and a pulse energy of 50 μJ. These are attenuated and are launched into the central core of a fiber array. The pulse $E_{sig}(x,y,t)$ which is leaving the array, is imaged onto an InGaAs camera, which is sensitive in this spectral region, and on a 10-μm thin BBO crystal, which is cut and is oriented for collinear broadband sum-frequency generation of light at λ_P and $\lambda_0 \pm 250$ nm. The InGaAs camera is used to record the time-averaged spatial profile of the wave packet at the end of the sample $I_{InGaAs}(x,y) = \int |E_{sig}(x,y,t)|^2 dt$.

The signal is propagating through the BBO crystal collinearly with the remaining 10% of the pump, which has a beam diameter much larger than the pitch of the array's image. The relative delay between the pulses is tunable using a motion stage with a relative resolution of $\Delta\tau < 6$ fs. The generated sum-frequency field at $\lambda_{SF} \approx 527$ nm can be approximated by [43,44]

$$I_{SF}(x,y,\tau) \sim \int |E_{sig}(x,y,t)|^2 |E_p(t-\tau)|^2 dt, \quad \text{(A1)}$$

which means that the signal recorded by the CCD camera is proportional to the intensity of the signal field convoluted with the pump pulse at the time slice defined by the delay τ between pump and pulse. Because the pump beam is roughly 60-fs long, one essentially records the intensity of the signal field with this resolution. Equation (A1) is valid under the assumptions of (i) nondepletion of the signal and pump, verified by the fact that the sum-frequency power is much lower then either signal or pump, (ii) negligible effects of dispersion and walk-off in the crystal, ensured by the small thickness of the crystal, (iii) spatial homogeneousness of the pump pulse, ensured by a large beam diameter, and (iv) a sufficiently broad range of phase-matched wavelengths—in our case, a range of 500 nm.

The spatiotemporal imaging scheme can be augmented further by placing interference filters with a bandwidth of $\Delta\lambda_{IF} = 10$ nm centered at $\lambda_{IF} = 510\cdots560$ nm between the BBO crystal and the CCD camera. After recording a series of spatiotemporal intensity images, one for each filter, one gets a spatiotemporal XFROG [55,56] trace $I_{SF}(x,y,\tau,\lambda)$, where $\lambda^{-1} = -\lambda_P^{-1} + \lambda_{IF}^{-1}$, giving full insight into the spatiotemporal structure of the light field with a spectral resolution of

$$\Delta\lambda = (\lambda/\lambda_{IF})^2 \Delta\lambda_{IF} \approx 86 \text{ nm}. \quad \text{(A2)}$$

This resolution is not yet high enough for model-free reconstruction of the spatiotemporal phase by means of an XFROG algorithm. The spectral range of the XFROG trace is limited by the bandwidth of the BBO crystal to 1350 nm $< \lambda <$ 1870 nm. Nonetheless, even at low time-frequency resolution, the XFROG setup allows a clear picture of the essential features of the LB dynamics in the waveguide array.

APPENDIX B: RECALL DISCRETE-CONTINUOUS LBS

Nonlinear evolution of light under the influence of the Kerr nonlinearity in a waveguide array is usually described in terms of the normalized discrete-continuous spatiotemporal NLSE [19]. This description is simplified especially in the femtosecond regime because it does not take higher-order linear or nonlinear terms into account. Nevertheless, the understanding of the solutions of this model is a great conceptual tool for the interpretation of the experiments and the results of the simulation of the full model discussed in Appendix C. The normalized NLSE reads as

$$
\begin{aligned}
i\frac{\partial A_{nm}(T,Z)}{\partial Z} = {} & \frac{\partial^2 A_{nm}(T,Z)}{\partial T^2} + |A_{nm}(T,Z)|^2 A_{nm}(T,Z) \\
& + A_{n\pm1m}(T,Z) + A_{nm\pm1}(T,Z) \\
& + A_{n\pm1m\pm1}(T,Z),
\end{aligned} \quad \text{(B1)}
$$

where $Z = cz$ is the normalized propagation length, $T = (c/\beta_2)^{1/2}t$ is the normalized time in the moving reference frame, and $A_{nm}(T) = (c/\gamma)^{1/2}a_{nm}(t)$ is the normalized amplitude such that $P_{nm} = |A_{nm}|^2$ is the power in the waveguide denoted by the indices n and m normalized to its physical counterpart $p = c/\gamma P$. $E = \sum_{nm} \int P_{nm} dt$ is the energy in the array normalized to the physical energy $e = (c\beta_2)/\gamma E$. The nonlinear coefficient $\gamma = 2\pi n_2(\lambda A_{eff})^{-1}$ of the array depends on the nonlinear constant of the material, which is $n_2 = 2.7 \cdot 10^{-20}$ m^2/W for silica [1], and the modal area is $A_{eff} = [\int dr_\perp |e(r_\perp)|^2]^2 / \int dr_\perp |e(r_\perp)|^4$ which can be derived from the shape of the Bloch modes $|e(r_\perp)|$ in the unit cell. The indices n and m denote the index of the waveguide.

Properties of the family of stationary solutions $A_{nm}(Z) = A_{nm}^{(stat)} \exp(ibZ)$ of Eq. (B1), depending on the nonlinearly induced shift of the wave number b, are displayed in Fig. 2 and are discussed in Sec. II. The discrete approximation of Eq. (B1) breaks down when the transversal structure of the linear eigenmodes is considerably altered by the nonlinearity, as discussed in Ref. [57]. b_{crit} can be estimated from the relation to the peak power P, as seen in Fig. 2(d). Then, the breakdown of Eq. (B1) is determined by the intensity that leads to a nonlinear index modulation on the order of

the geometrical index modulation Δn, thus, $\Delta n = n_2 I_{\mathrm{crit}} = n_2 A_{\mathrm{eff}}^{-1} c \gamma^{-1} P_{\mathrm{crit}} = c \lambda / (2\pi) P_{\mathrm{crit}}$ Therefore,

$$P_{\max} \ll P_{\mathrm{crit}} = \Delta n \frac{2\pi}{\lambda c}. \qquad (B2)$$

Inequality (B2) gives a value of $P_{\max} \ll 150$, which, for values taken from Fig. 1 at $\lambda = 1550$ nm, translates into a real-world peak power,

$$p_{\max} \ll p_{\mathrm{crit}} = \Delta n \frac{2\pi}{\lambda \gamma}, \qquad (B3)$$

which is roughly $p_{\max} \ll 6$ MW. If compared to the power of a purely spatial Townes soliton [58] $p_{\mathrm{Townes}} = 5.32 n \lambda (2\pi n_2)^{-1}$ this yields a relation, between the two, of

$$\alpha = \frac{p_{\max}}{p_{\mathrm{Townes}}} < \frac{4\pi^2 \Delta n \cdot n A_{\mathrm{eff}}}{10.6 \, \lambda^2}. \qquad (B4)$$

For the values discussed here, we get $\alpha_{1550 \, \mathrm{nm}} \approx 1.5$ and more for longer wavelengths due to the growth of A_{eff}. Thus, the peak power of a LB can exceed the peak power of a Townes soliton, which is due to the dispersion that additionally has to be balanced by the nonlinearity. The breakdown of Eq. (B1) is typically related to a destabilization of the solutions as previously discussed in Refs. [19,57], thus, we find a window of stable LBs.

APPENDIX C: EXTENDED EQUATIONS AND NUMERICAL TREATMENT

One consequence of the upper temporal bound discussed in Sec. II is that the realistic description of an experiment involving LBs, which are on the scale of just a few optical cycles and, thus, extremely broadband, Eq. (B1) is insufficient. It needs to be refined to include the wavelength dependence of the discrete coupling and the dispersion. The noninstantaneous nature of the nonlinear response is addressed, including the Raman- and self-steepening responses of the medium. Furthermore, it does not make sense to apply the slowly varying envelope approximation. A realistic model for the propagation of such ultrashort pulses in nonlinear media is the set of coupled unidirectional Maxwell equations described in Ref. [38] augmented by the nonlinear noninstantaneous response function of silica described in Ref. [1],

$$-i \, \mathrm{sgn}(\omega) \frac{\partial}{\partial z} E_{nm}(z, \omega)$$
$$= [\beta(\omega) - \omega \beta_1] E_{nm}(z, \omega)$$
$$+ c(\omega) \sum_{n'm'} C_{nm}^{n'm'} E_{n'm'}(z, \omega) + \frac{4}{3} \gamma P_{nm}^{\mathrm{NL}}(z, \omega),$$

$$P_{nm}^{\mathrm{NL}}(z, t) = E_{nm}(z, t) \Big[(1 - f) E_{nm}(z, t)^2 \qquad (C1)$$
$$+ f \int E_{nm}(z, t - t')^2 h(t') dt' \Big],$$

$$h(t) = \begin{cases} 0, & t < 0, \\ \dfrac{\tau_1^2 + \tau_2^2}{\tau_1 \tau_2^2} \exp(-t/\tau_2) \sin(t/\tau_1), & t \geqslant 0, \end{cases}$$

where $E_{nm}(z, \omega)$ is the square root of the instantaneous optical power of a given carrier frequency in the core denoted by the index nm, $\beta_1 = d\beta(\omega)/d\omega|_{\omega = \omega_0}$ is the inverse velocity of

the comoving reference frame, $\mathrm{sgn}(\omega)$ is the sign function, $C_{nm}^{n'm'}$ is a matrix, which is either 1, if the cores denoted by the indices nm and $n'm'$ are nearest neighbors, or is 0 otherwise. The nonlinear parameter γ is the same as in the last section. $P_{nm}^{\mathrm{NL}}(z, t)$ is the nonlinear response, evaluated in time and includes the contribution from the Kerr and the Raman effects. The quantities $f = 0.22$, $\tau_1 = 12.2$ fs, and $\tau_2 = 32$ fs characterize the contribution of the delayed response, its frequency shift, and its delay time, taken from tabulated data in Ref. [1].

Equation (C1) is solved by a modified split-step Fourier algorithm. The linear part is solved by transformation of $E_{nm}(z, \omega)$ into the eigenspace of the coupling matrix $C_{nm}^{n'm'}$. The nonlinear contribution is included, with a fourth-order Runge-Kutta scheme, where $E_{nm}(z, t)$ is acquired by Fourier transformation of $E_{nm}(z, \omega)$ and the convolution operation is again carried out in Fourier space of $E_{nm}(z, t)^2$ Note that, due to the reality of the electric fields $E_{nm}(z, t) \in \mathbb{R}$ one only calculates the Fourier components with positive frequencies as $E_{nm}(z, \omega) = E_{nm}^*(z, -\omega)$

APPENDIX D: SCALING OF PROPAGATION LENGTH

The length of self-confined propagation L_{LB} is mainly determined by the rate of Raman-redshift $L_{\mathrm{LB}} \sim [d\Delta\omega(z)/dz]^{-1}$ which depends on the LB's width T_0 and peak power P_0 and can be derived by treating the Raman contribution as a perturbation to the solutions of Eq. (B1), with

$$\frac{\partial A_{nm}(t, z)}{\partial z} = Q(A) - i \gamma T_R \left(A \frac{\partial |A|^2}{\partial t} \right), \qquad (D1)$$

where $Q(A)$ is the part of the equation given by Eq. (B1) and $A_{nm}^{(b)}(t) = A_{nm}(t, z) \exp(ibz)$ are its stationary solutions, which are assumed to vary locally around a given b_0 such that $A_{nm}^{(b)}(t) \approx P_0^{1/2} A_{nm}^{(b_0)}(t/T_0)$ with a given scaling $P_0 = T_0^{\alpha(b_0)}$ determined by the stationary solutions of Eq. (B1). Thus, the local shape $A_{nm}^{(b)}$ does depend only weakly on b. Then, the rate of self-induced frequency change can be determined by plugging the ansatz $A_{nm}(t, z = 0) = A_{nm}^{(b)}(t) \exp[-i\Delta\omega(z)t]$ into Eq. (D1), yielding

$$\frac{d\Delta\omega(z)}{dz} = 2\gamma T_R f^{(b)} \frac{P_0}{T_0^2}, \qquad (D2)$$

where $f^{(b)} = \sum_{nm} \int x^{-1} [A_{nm}^{(b)}(x)]^3 A_{nm}'^{(b)}(x) dx / \sum_{nm} \int (A_{nm}^{(b)}(x))^2 dx$ $f^{(b)}$ depends on the local shape of the LB solution but does not explicitly contribute to the scaling of L_{LB}, which is $L_{\mathrm{LB}} \sim T_0^2 P_0^{-1}$.

The ratio between these two quantities depends directly on the local slope dimensionality [57],

$$d_{\mathrm{slope}} = 2 \left(1 - \frac{b}{E} \frac{dE}{db} \right), \qquad (D3)$$

of the LB solution, which can be taken from the slope of

Fig. 2(a) or Fig. 2(d). The stable branch of the LB solutions extends from the turning point with $dE/db = 0$ and, thus, $d_{slope} \leqslant 2$ to peak power solutions, for which the spatial dynamics is strong decoupled, yielding $d_{slope} \geqslant 1$. These two extremes yield $P_0 \sim T_0^{-1}$ and $P_0 \sim T_0^{-2}$, respectively. If one further takes into account that $T_0 \sim c^{-1/2}$ [see Fig. 2(b)] and measures L_{LB} in units of L_{Disp}, in turn, being proportional to

T_0^2, it follows that

$$\frac{L_{LB}}{\langle L_{Disp} \rangle} \sim c^{-q} \quad \frac{1}{2} < q < 1. \quad (D4)$$

As a consequence, this proves that reduction of the coupling strength will extend the LB lifetime but only does so at a very moderate rate.

[1] G. Agrawal, *Nonlinear Fiber Optics* (Academic, San Diego, 2001).

[2] Y. Kivshar and G. Agrawal, *Optical Solitons* (Academic, San Diego, 2003).

[3] R. Alfano, *The Supercontinuum Laser Source: Fundamentals with Updated References* (Springer, Berlin, 2006).

[4] L. F. Mollenauer and R. H. Stolen, Opt. Lett. **9**, 13 (1984).

[5] D. Solli, C. Ropers, P. Koonath, and B. Jalali, Nature (London) **450**, 1054 (2007).

[6] A. Hasegawa and F. Tappert, Appl. Phys. Lett. **23**, 142 (1973).

[7] L. F. Mollenauer, R. H. Stolen, and J. P. Gordon, Phys. Rev. Lett. **45**, 1095 (1980).

[8] J. J. Rasmussen and K. Rypdal, Phys. Scr. **33**, 481 (1986).

[9] Y. Silberberg, Opt. Lett. **15**, 1282 (1990).

[10] G. Fibich and B. Ilan, Opt. Lett. **29**, 887 (2004).

[11] L. Bergé, Phys. Rep. **303**, 259 (1998).

[12] S. Adhikari, Phys. Rev. E **70**, 36608 (2004).

[13] H. C. Gurgov and O. Cohen, Opt. Express **17**, 7052 (2009).

[14] I. B. Burgess, M. Peccianti, G. Assanto, and R. Morandotti, Phys. Rev. Lett. **102**, 203903 (2009).

[15] F. Lederer *et al.*, Phys. Rep. **463**, 1 (2008).

[16] S. K. Turitsyn, Opt. Lett. **18**, 1493 (1993).

[17] A. B. Aceves and C. D. Angelis, Opt. Lett. **18**, 110 (1993).

[18] Y. Kivshar and S. Turitsyn, Phys. Rev. E **49**, 2536 (1994).

[19] D. Mihalache *et al.*, Phys. Rev. E **70**, 055603 (2004).

[20] X. Liu, L. J. Qian, and F. W. Wise, Phys. Rev. Lett. **82**, 4631 (1999).

[21] A. V. Buryak, P. D. Trapani, D. V. Skryabin, and S. Trillo, Phys. Rep. **370**, 63 (2002).

[22] O. Martinez, IEEE J. Quantum Electron. **25**, 2464 (1989).

[23] P. Di Trapani *et al.*, Phys. Rev. Lett. **81**, 570 (1998).

[24] P. Di Trapani *et al.*, Phys. Rev. Lett. **91**, 093904 (2003).

[25] J. Trull *et al.*, Phys. Rev. E **69**, 026607 (2004).

[26] D. Faccio *et al.*, J. Opt. Soc. Am. B **22**, 862 (2005).

[27] A. Couairon, Eur. Phys. J. **27**, 159 (2003).

[28] A. Chong, W. Renninger, D. Christodoulides, and F. Wise, Nature Photon. **4**, 103 (2010).

[29] D. Abdollahpour, S. Suntsov, D. G. Papazoglou, and S. Tzortzakis, Phys. Rev. Lett. **105**, 253901 (2010).

[30] S. Jia, W. Wan, and J. Fleischer, Phys. Rev. Lett. **99**, 223901 (2007).

[31] M. Heinrich *et al.*, Phys. Rev. Lett. **103**, 113903 (2009).

[32] A. Szameit *et al.*, Opt. Express **14**, 6055 (2006).

[33] D. Christodoulides and R. Joseph, Opt. Lett. **13**, 794 (1988).

[34] H. Eisenberg, Y. Silberberg, R. Morandotti, A. Boyd, and J. Aitchison, Phys. Rev. Lett. **81**, 3383 (1998).

[35] J. Fleischer, M. Segev, N. Efremidis, and D. Christodoulides, Nature (London) **422**, 147 (2003).

[36] T. Pertsch *et al.*, Phys. Rev. Lett. **93**, 53901 (2004).

[37] C. J. Benton, A. V. Gorbach, and D. V. Skryabin, Phys. Rev. A **78**, 033818 (2008).

[38] I. Babushkin, A. Husakou, J. Herrmann, and Y. S. Kivshar, Opt. Express **15**, 11978 (2007).

[39] H. Eisenberg *et al.*, Phys. Rev. Lett. **87**, 43902 (2001).

[40] F. Wise and P. D. Trapani, Opt. Photonics News **13**, 28 (2002).

[41] D. Cheskis *et al.*, Phys. Rev. Lett. **91**, 223901 (2003).

[42] S. Minardi *et al.*, Phys. Rev. Lett. **91**, 123901 (2003).

[43] M. A. C. Potenza *et al.*, Opt. Commun. **229**, 381 (2004).

[44] S. Minardi, J. Trull, and M. A. C. Potenza, J. Holography Speckle **5**, 85 (2009).

[45] S. Minardi *et al.*, Phys. Rev. Lett. **105**, 263901 (2010).

[46] U. Röpke, H. Bartelt, S. Unger, K. Schuster, and J. Kobelke, Opt. Express **15**, 6894 (2007).

[47] U. Röpke, H. Bartelt, S. Unger, K. Schuster, and J. Kobelke, Appl. Phys. B: Lasers and Optics, doi:10.1007/s00340-011-4635-8

[48] P. W. Anderson, Phys. Rev. **109**, 1492 (1958).

[49] T. Schwartz, G. Bartal, S. Fishman, and M. Segev, Nature (London) **446**, 52 (2007).

[50] A. Szameit *et al.*, Appl. Phys. B: Lasers Opt. **82**, 507 (2006).

[51] N. Vakhitov and A. Kolokolov, Radiophys. Quantum Electron. **16**, 783 (1973).

[52] M. Kolesik and J. V. Moloney, Phys. Rev. E **70**, 036604 (2004).

[53] P. Kinsler, Phys. Rev. A **81**, 023808 (2010).

[54] H. De Raedt, A. Lagendijk, and P. de Vries, Phys. Rev. Lett. **62**, 47 (1989).

[55] R. Trebino, *Frequency-Resolved Optical Gating: The Measurement of Ultrashort Laser Pulses* (Kluwer Academic, Dordrecht, 2002).

[56] S. Linden, H. Giessen, and J. Kuhl, Phys. Status Solidi B **206**, 119 (1998).

[57] F. Eilenberger, A. Szameit, and T. Pertsch, Phys. Rev. A **82**, 043802 (2010).

[58] R. Y. Chiao, E. Garmire, and C. H. Townes, Phys. Rev. Lett. **13**, 479 (1964).

[59] See Supplemental Material at http://link.aps.org/supplemental/10.1103/PhysRevA.84.013836, Media 1) Experimental cross-correlation traces for varying input fibre of a sample with $L_{Diff} = 22$ mm and a lnegth of $L = 20$ mm. Media 2) Experimental cross-correlation traces for varying input fibre of a sample with $L_{Diff} = 22$ mm and a lnegth of $L = 60$ mm. Media 3) LB evolution in central waveguide for a sample with $L_{Diff} = 22$ mm. Media 4) LB evolution in central waveguide for a sample with $L_{Diff} = 96$ mm.